ATOMS: ALMA Three-millimeter Observations of Massive Star-forming regions - XI. From inflow to infall in hub-filament systems

Jian-Wen Zhou, Tie Liu, Neal J. Evans, Guido Garay, Paul F. Goldsmith, Gilberto C. Gómez, Enrique Vázquez-Semadeni, Hong-Li Liu, Amelia M. Stutz, Ke Wang, et al.

HAL Id: insu-03867453

https://insu.hal.science/insu-03867453

Submitted on 7 Apr 2023

ATOMS: ALMA Three-millimeter Observations of Massive Star-forming regions – XI. From inflow to infall in hub-filament systems

Jian-Wen Zhou,[1,2]⋆ Tie Liu,[3]⋆ Neal J. Evans, II,[4] Guido Garay,[5] Paul F. Goldsmith,[6] Gilberto C. Gómez,[7] Enrique Vázquez-Semadeni,[7] Hong-Li Liu [ORCID],[8] Amelia M. Stutz,[9] Ke Wang,[10] Mika Juvela,[11] Jinhua He,[12,13,14] Di Li,[1,2,15] Leonardo Bronfman,[14] Xunchuan Liu,[3] Feng-Wei Xu [ORCID],[10,16] Anandmayee Tej,[17] L. K. Dewangan [ORCID],[18] Shanghuo Li,[19] Siju Zhang,[10] Chao Zhang,[20] Zhiyuan Ren [ORCID],[1] Ken'ichi Tatematsu [ORCID],[21,22] Pak Shing Li,[23] Chang Won Lee,[19,24] Tapas Baug,[25] Sheng-Li Qin,[8] Yuefang Wu,[16] Yaping Peng,[26] Yong Zhang,[27,28,29] Rong Liu,[1,2] Qiu-Yi Luo,[2,3] Jixing Ge,[13] Anindya Saha,[17] Eswaraiah Chakali,[30] Qizhou Zhang,[31] Kee-Tae Kim,[19] Isabelle Ristorcelli,[32] Zhi-Qiang Shen[3] and Jin-Zeng Li[1]

Affiliations are listed at the end of the paper

ABSTRACT

We investigate the presence of hub-filament systems in a large sample of 146 active proto-clusters, using $H^{13}CO^+$ J = 1-0 molecular line data obtained from the ATOMS survey. We find that filaments are ubiquitous in proto-clusters, and hub-filament systems are very common from dense core scales ($\sim$0.1 pc) to clump/cloud scales ($\sim$1–10 pc). The proportion of proto-clusters containing hub-filament systems decreases with increasing dust temperature (T_d) and luminosity-to-mass ratios (L/M) of clumps, indicating that stellar feedback from H II regions gradually destroys the hub-filament systems as proto-clusters evolve. Clear velocity gradients are seen along the longest filaments with a mean velocity gradient of 8.71 km s^{-1} pc^{-1} and a median velocity gradient of 5.54 km s^{-1} pc^{-1}. We find that velocity gradients are small for filament lengths larger than $\sim$1 pc, probably hinting at the existence of inertial inflows, although we cannot determine whether the latter are driven by large-scale turbulence or large-scale gravitational contraction. In contrast, velocity gradients below $\sim$1 pc dramatically increase as filament lengths decrease, indicating that the gravity of the hubs or cores starts to dominate gas infall at small scales. We suggest that self-similar hub-filament systems and filamentary accretion at all scales may play a key role in high-mass star formation.

Key words: ISM: clouds – ISM: H II regions – ISM: kinematics and dynamics – stars: formation – stars: protostars.

1 INTRODUCTION

Filamentary structures are ubiquitous in high-mass star-forming molecular clouds. Their relation with massive star formation is not yet understood. According to previous studies, a collapsing cloud with converging filaments forms a hub-filament system (HFS). HFSs are known as a junction of three or more filaments. Filaments have lower column densities compared to the hubs, but filaments show much higher aspect ratio than the hubs (Myers 2009; Schneider et al. 2012). In such systems, converging flows are funnelling matter into the hub through the filaments. Many case studies have suggested that HFSs are birth cradles of high-mass stars and clusters (Peretto et al. 2013; Henshaw et al. 2014; Zhang et al. 2015; Liu et al. 2016a; Lu et al. 2018; Yuan et al. 2018; Liu, Stutz & Yuan 2019; Dewangan et al. 2020). In HFSs, cores embedded in denser clumps can prolong the accretion time for growing massive stars due to the sustained supply of matter from the filamentary environment (Myers 2009). Numerical simulations of colliding flows and collapsing turbulent clumps show that massive protostars grow from low-mass stellar seeds by feeding gas along the dense filamentary streams converging towards the $\sim$0.1 pc size hubs with detectable velocity gradients along the filaments (Wang et al. 2010; Gómez & Vázquez-Semadeni 2014; Smith et al. 2016; Padoan et al. 2020). To date, however, only a few spectral line observations have been conducted to investigate accretion flows along filaments (Liu et al. 2012, 2019; Kirk et al. 2013; Peretto et al. 2013; Lu et al. 2018; Chen et al. 2019; Chung et al. 2019, 2021).

To deepen our understanding of high-mass star formation in HFSs, it is necessary to obtain kinematic information on scales down to $\sim$0.1 pc, similar to studies in nearby clouds (André et al. 2014, 2016). Such high-spatial resolution observations towards massive filaments, however, are still rare, and most previous studies are case studies towards infrared dark clouds (Wang et al. 2011; Peretto et al. 2013; Henshaw et al. 2014; Beuther et al. 2015; Zhang et al. 2015; Busquet et al. 2016; Ohashi et al. 2016; Lu et al. 2018; Li et al. 2022; Liu et al. 2022a, b). Therefore, it is crucial to study the properties of HFSs and investigate how these systems evolve from a statistical view with a large sample.

⋆ E-mail: zjw@nao.cas.cn (JWZ); liutie@shao.ac.cn (TL)

To this end, here we conduct a statistical study of a large HF sample across various evolutionary phases for investigating the relation between HFs and high-mass star formation using the $H^{13}CO^+$ J = 1-0 molecular line data from ALMA Three-millimeter Observations of Massive Star-forming regions (ATOMS) survey (Liu et al. 2020a). We describe the detailed observations and data used in this paper in Section 2. The identification and properties of HFs are presented in Section 3, and the role of HFSs in high-mass star formation is discussed in Section 4. We summarize our results in Section 5.

2 OBSERVATIONS

2.1 ALMA observations

We use ALMA data from the ATOMS survey (Project ID: 2019.1.00685.S; PI: T. Liu). The details of the 12- and 7-m array ALMA observations were summarized in Liu et al. (2020a, 2021). Calibration and imaging were carried out using the CASA software package version 5.6 (McMullin et al. 2007). The 7-m data and 12-m array data were calibrated separately. Then the visibility data from the 7- and 12-m array configurations were combined and later imaged in CASA. For each source and each spectral window (spw), a line-free frequency range is automatically determined using the ALMA pipeline (see ALMA technical handbook). This frequency range is used to (i) subtract continuum from line emission in the visibility domain, and (ii) make continuum images. Continuum images are made from multifrequency synthesis of data in this line-free frequency ranges in the two 1.875-GHz wide spws, spw 7 and 8, centred on ~99.4 GHz (or 3 mm). Visibility data from the 12- and 7-m array are jointly cleaned using task tclean in CASA 5.6. We used natural weighting and a multiscale deconvolver, for an optimized sensitivity and image quality. All images are primary-beam corrected. The continuum image reaches a typical 1σ rms noise of ~0.2 mJy in a synthesized beam full width at half-maximum (FWHM) size of ~2.2 arcsec. In this work, we also use $H^{13}CO^+$ J = 1-0 (86.754288 GHz) line data with a spectral resolution of 0.211 km s^{-1}. The typical beam FWHM size and channel rms noise level for $H^{13}CO^+$ J = 1-0 line emission are ~2.5 arcsec and 8 mJy beam^{-1}, respectively. The typical maximum recovered angular scale in this survey is about 1 arcmin, which is comparable to the size of field of view (FOV) in 12-m array observations (Liu et al. 2020a). Therefore, missing flux should not be a big issue for gas kinematics studies in this work, even though total-power observations were not included.

2.2 Spitzer infrared data

We also use images at 3.6, 4.5, 5.8, and 8.0 μm, obtained by the *Spitzer* Infrared Array Camera (IRAC), as part of the GLIMPSE project (Benjamin et al. 2003). The images of IRAC were retrieved from the *Spitzer* Archive and the angular resolutions of images are better than 2 arcsec.

2.3 Numerical simulation data

We compared the observational data to one of the filaments described in Gómez & Vázquez-Semadeni (2014). Those authors studied the structure and dynamics of filaments formed in a molecular cloud modelled using the GADGET-2 smoothed particle hydrodynamics (SPH) code modified to include the cooling function proposed by Koyama & Inutsuka (2002, as corrected for typographical errors by Vázquez-Semadeni et al. 2007). The simulation set-up is a high-resolution version of the one presented in Vázquez-Semadeni et al.

(2007), which consisted of two transonic streams moving in opposite directions in a medium of constant density (1 cm^{-3}) corresponding to the warm neutral medium, in a numerical box of 256 pc per side. The high-resolution simulation of Gómez & Vázquez-Semadeni (2014) had 296^3 SPH particles, each with a mass of 0.02 M$_\odot$, and a total mass of 5.18 × 10^5 M$_\odot$. The compression generated by these converging flows induces a phase transition in the gas to the cold neutral medium, so that the Jeans mass of the dense layer decreases by a factor of 10^4 and its subsequent gravitational collapse is nearly pressure-less. The layer experiences hydrodynamical instabilities (Vishniac 1994; Walder & Folini 2000; Heitsch et al. 2005, 2006; Vázquez-Semadeni et al. 2006) due to the ram-pressure confinement exerted by the flow, causing moderately supersonic turbulent motions within the layer. Additionally, this flow increases the layer's mass as it collapses, eventually reaching > 5 × 10^4 M$_\odot$.

Pressure-less gravitational collapse of spheroids proceeds along their shortest dimension first (Lin, Mestel & Shu 1965). Thus, three-dimensional (3D) structures collapse into sheets and these in turn collapse into filaments. Therefore, the filaments themselves in this simulation are produced by gravity-driven motions. Gómez & Vázquez-Semadeni (2014) report filaments of ~15 pc and ~600 M$_\odot$ when a density threshold of 10^3 cm^{-3} is used to define them. These filaments are not material, but *flow structures* able to exist for times longer than their flow-crossing time, since they are continuously replenished by their surroundings, lower density cloud gas. They are able to reach a quasi-steady state because the accreted material is evacuated along their longitudinal direction, on to the clumps that are formed within the filaments or at the positions where two or more filaments meet. These authors interpret this longitudinal flow (~0.5 km s^{-1} in their simulations) as a signature of the global hierarchical collapse (GHC) model for molecular clouds (Vázquez-Semadeni et al. 2019). The simulation set-up (compression-induced phase transition in the neutral medium) ensures that the turbulent flow generated by the instabilities and gravitational collapse, together with the resulting non-linear density fluctuations, are fully self-consistent, thus avoiding the possibility of artificially supporting the cloud against collapse due to overdriven turbulence injection or spatially mismatched velocity and density structures. This self-consistency is fundamental for the study of the flow into and along dense filaments.

3 RESULTS

3.1 Filaments identified by $H^{13}CO^+$ J = 1-0

3.1.1 $H^{13}CO^+$ J = 1-0 as a probe for dense gas

We use $H^{13}CO^+$ J = 1-0 line data to identify filaments in the ATOMS sources. $H^{13}CO^+$ J = 1-0 has a rather high critical density of 6.2×10^4 cm^{-3} at 10 K. Because its optical depth is much lower than its main-line counterpart HCO$^+$ J = 1-0, its effective excitation density is not much less ($n_{eff} = 3.9 \times 10^4$ cm^{-3}) (Bergin & Tafalla 2007; Shirley 2015). These features make it a good tracer of dense gas. Moreover, Shimajiri et al. (2017) found that the spatial distribution of the $H^{13}CO^+$ (1-0) emission is tightly correlated with the column density of the dense gas revealed by *Herschel* data. In particular, the $H^{13}CO^+$ J = 1-0 emission traces the dense 'supercritical' filaments detected by *Herschel* very well (Shimajiri et al. 2017). The virial mass estimates derived from the velocity dispersion of $H^{13}CO^+$ J = 1-0 also agree well with the dense gas mass estimates derived from *Herschel* data for the same subregions (Shimajiri et al. 2017). In particular, the $H^{13}CO^+$ J = 1-0 spectra over the mapping areas (except the very dense regions) of the majority (~75 per cent) of
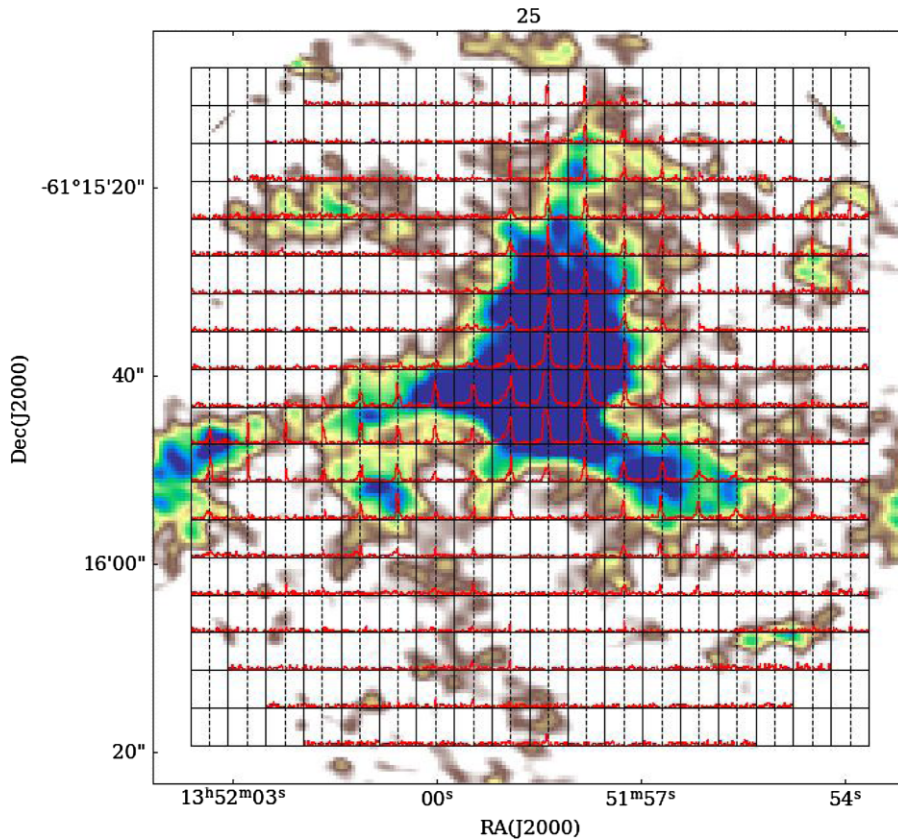
Figure 1. The $H^{13}CO^+$ spectral grid map for an exemplar source. The background image shows the integrated intensity map. The grid maps of $H^{13}CO^+$ for all of ATOMS sources are available as supplementary material.

sources in the ATOMS sample are singly peaked (see Fig. 1). As shown in Fig. 2, we find that $H^{13}CO^+$ J = 1-0 ATOMS data trace the whole morphology of HFs well.

3.1.2 Identification of filaments

We use the moment 0 maps (integrated intensity maps) rather than channel maps of $H^{13}CO^+$ J = 1-0 to identify filaments in ATOMS sources because: (i) ATOMS sources do not show multiple velocity components with velocity differences larger than 10 km s^{-1} for dense gas tracers (see Fig. 1), which would be attributed to foreground or background cloud emission (Liu et al. 2016b); (ii) integrated intensity maps have much better sensitivity for identifying fainter gas structures than channel maps; (iii) we are interested in the overall HF structures rather than their internal fine structures, which may not always be real density enhancements in space due to the complex velocity field (Zamora-Avilés, Ballesteros-Paredes & Hartmann 2017) and are also not well resolved in our observations.

The velocity intervals for making moment 0 maps are determined from the averaged spectra (radius ~25 arcsec) of $H^{13}CO^+$ J = 1-0, where the intensity of averaged spectra decreases to zero. This limits the typical velocity range within ~±5 km s^{-1} around the systemic velocity for most sources. Moreover, a threshold of 5σ is applied to make the moment maps, which can reduce the noise contamination effectively.

We used the FILFINDER algorithm (Koch & Rosolowsky 2015) to identify filaments from the moment 0 maps of $H^{13}CO^+$ (1-0). We set the same parameters of FILFINDER for all sources in the first run. However, since the signal-to-noise levels of $H^{13}CO^+$ J = 1-

0 emission vary within different sources, we carefully adjust the parameters for individual sources in further identification. We note that the structures identified by FILFINDER change only slightly when we adjust the parameters. The skeletons of identified filaments overlaid on the moment-0 maps of $H^{13}CO^+$ J = 1-0 line emission are shown in Fig. 2 and in supplementary material. The filament skeletons identified by FILFINDER are highly consistent with the gas structures traced by $H^{13}CO^+$ J = 1-0 as seen by eye, indicating that the structures identified in FILFINDER are very reliable. At a first glance of these maps, filaments are nearly ubiquitous in 139 ATOMS proto-clusters. Filaments are not seen in only six ATOMS sources; in all six, the $H^{13}CO^+$ J = 1-0 line emission was weak or undetected. These six sources may not contain dense gas with densities high enough to excite $H^{13}CO^+$ J = 1-0 line emission.

3.2 HFSs in massive proto-clusters

In this work, a strictly defined HFS has following properties: (i) at least three filaments are intertwined; and (ii) the brightest 3 -mm continuum core is penetrated by the longest filament, and is close to (<1 beam size) the junction region, called the hub, where is the centre of the gravity potential well and potential site for high-mass star formation.

The brightest 3-mm continuum cores in hub regions could be associated with compact H II regions or even younger (ultra-compact and hyper-compact) H II regions or high-mass protostars, which are still deeply embedded in molecular gas (see Fig. 2). Clumps associated with more evolved and extended H II regions that look like infrared bubbles in *Spitzer* 8-μm emission maps (see Fig. 3) are
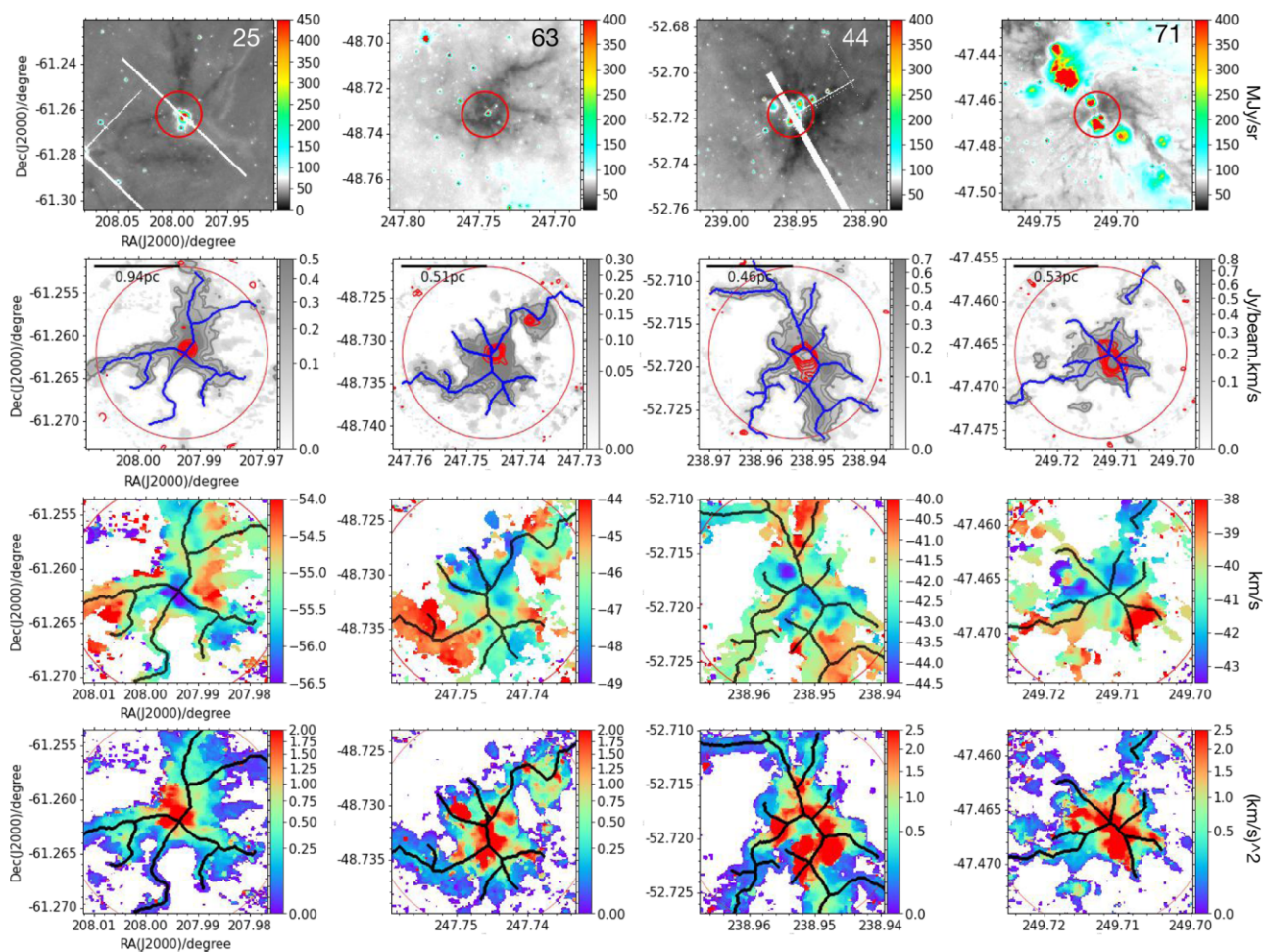
Figure 2. HFSs in four exemplar sources. The first row shows the colour images of *Spitzer* 8-μm emission. The source numbers in the upper-right corners are from the table A1 of Liu et al. (2020a). The second row displays the filaments (blue lines) identified in the moment 0 maps (background) of $H^{13}CO^+$ J = 1-0. The red contours represent 3-mm continuum emission, with lowest contour 5σ. The third and fourth rows show the moment 1 and 2 maps of $H^{13}CO^+$ J = 1-0 with filament skeletons shown in black lines. The radius of red circles in the maps is 36 arcsec, which corresponds to the FOV of the ALMA observations. The moment 0 maps of $H^{13}CO^+$ J = 1-0 overlaid with filament skeletons for the other sources are available as supplementary material.

excluded in the classification of HFSs because these regions are more likely in expansion and are not gravitationally bound. In addition, their 3-mm continuum emission usually significantly deviates from the $H^{13}CO^+$ emission.

Fig. 2 presents the maps of four well-defined HFSs. These HFSs are connected to larger filamentary structures revealed by extinction in *Spitzer* 8-μm images (see top row of panels in Fig. 2). Although their velocity fields are complicated, most HFSs show clear velocity gradients as shown in the moment 1 maps of $H^{13}CO^+$ J = 1-0 (third row of Fig. 2). In addition, the velocity dispersion of $H^{13}CO^+$ J = 1-0 increases towards the hub regions (see bottom panels of Fig. 2).

In total, 49 per cent of the sources are classified as HFSs under our strict definition. This proportion is quite high, considering that the HF morphology of many sources may have been destroyed by stellar feedback. As discussed in Zhang et al. (2022), nearly 51 per cent of ATOMS sources show $H_{40\alpha}$ emission, a tracer for H II regions. The HFSs are likely destroyed quickly as H II regions expand (e.g. see sources in Fig. 3). The evolution of HFSs under stellar feedback will be discussed in detail below.

We note that our definition of HFSs is somehow very strict. If we only consider the first condition in the definition and ignore the second one, the fraction of HFSs in ATOMS sources can reach as

high as 80 per cent. To conclude, we find that HFSs are very common within massive proto-clusters.

3.2.1 HFSs at various spatial scales

ATOMS sources are at various distances from 0.4 to 13.0 kpc (see Fig. A1a), enabling us to investigate filaments from core scale (∼0.1 pc) to clump/cloud scale (several pc) under a uniform angular resolution (∼2 arcsec) with a large sample (Liu et al. 2020a). Fig. 4 shows the length distribution of the longest filaments in these sources. The length ranges from 0.086 to 4.87 pc with a mean value of 1.61 pc and a median value of 1.35 pc, indicating that filaments as well as HFSs can exist not only in small-scale (∼0.1 pc) dense cores but also in large-scale clumps/clouds (∼1–5 pc), and probably up to 10 pc, considering projection effects and the limited FOV of ALMA.

We have also noticed that there is no significant difference in the distribution of filament lengths between our strictly defined HFSs sample and the rest non-HFS sample. The possible reasons for this may be: (i) those non-HFS sources may also contain some 'hub'-like structures but cannot match our strict definition of HFS; (ii) those non-HFS sources may have had hubs in the past but their hubs have been destroyed by formed H II regions (cf. Section 3.2.2), however,
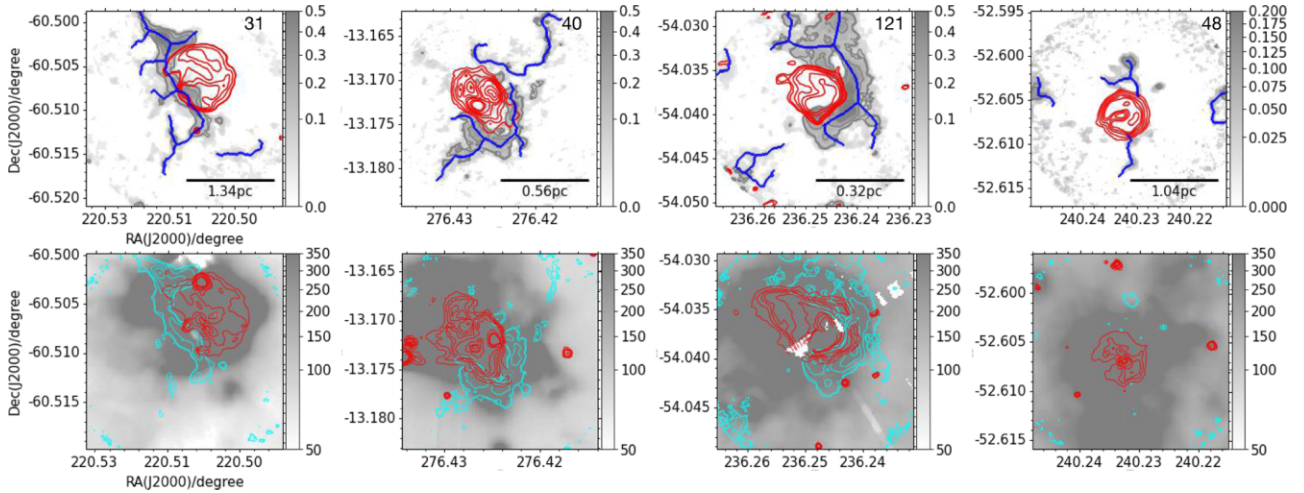
Figure 3. Four ATOMS sources containing expanding H II regions. The first row displays the filaments (blue lines) identified in the moment 0 maps (background) of $H^{13}CO^+$ (1-0). Red contours represent 3-mm continuum emission with its minimum contour level of 5σ. Background images in the second row show the *Spitzer* 8-μm emission, which traces the polycyclic aromatic hydrocarbon emission in PDRs of H II regions. The cyan and red contours show the moment 0 maps of $H^{13}CO^+$ (1-0) and the *Spitzer* 4.5-μm emission, respectively. The colour bars on the right indicate the flux scale in Jy beam^{-1} km s^{-1} for moment 0 maps and MJy sr^{-1} for *Spitzer* 8-μm emission. The moment 0 maps of $H^{13}CO^+$ J = 1-0 overlaid with filament skeletons for the other sources containing H II regions are available as supplementary material.
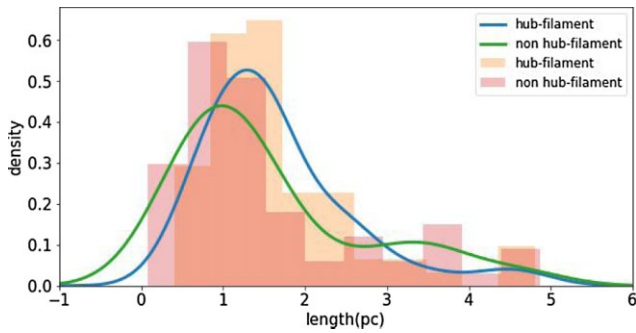

Figure 4. The length distribution of the longest filaments in ATOMS sources.

filaments themselves are still persistent; and (iii) we cannot rule out the possibility that those HFS sources are superpositions of filaments due to projection effect.

The ATOMS sources were initially selected from a complete and homogeneous CS J = 2-1 molecular line survey towards IRAS sources with far-infrared colours characteristics of UC H II regions (Bronfman, Nyman & May 1996). As discussed in Liu et al. (2020a), the ATOMS sources are distributed in very different environments of the Milky Way, and are an unbiased sample of the proto-clusters with the strongest CS J = 2-1 line emission ($T_A > 2$ K) located in the inner Galactic plane of $-80° < l < 40°$, $|b| < 2°$ (Faúndez et al. 2004). As discussed below, we think that most massive clumps should have had HFSs but their hubs can be gradually destroyed as H II regions form and evolve. Therefore, we suggest that self-similar HFSs at scales from ~ 0.1 to ~ 10 pc play a crucial role in massive cluster formation in various environments.

3.2.2 Evolution of HFSs

As massive proto-stars evolve, the dust temperature (T_d) and luminosity-to-mass ratio (L/M) of their natal clumps will increase.

Therefore, T_d and L/M are often used for the evolutionary classification of dense star-forming clumps (Saraceno et al. 1996; Molinari et al. 2008, 2019; Liu et al. 2016b, 2017; Stephens et al. 2016; Urquhart et al. 2018). We divide ATOMS sources into three uniformly spaced bins in T_d and L/M, respectively. We emphasize that T_d and L/M do not depend on distances in the sample (see Fig A1b and c). Considering the small dynamic range in T_d and L/M of the data, we did not divide the sample into more bins, in order to avoid potential misleading results (see Appendix A). Then we calculate the proportion of sources with HF morphology in each bin. As shown in Fig. 5, the proportion of HFSs decreases with increasing T_d and L/M, strongly indicating that HFSs are gradually destroyed as proto-clusters evolve.

Liu et al. (2021) identified all the dense cores in the ATOMS clumps and classified them based on their evolutionary stages (e.g. hot cores, UC H II regions). The evolutionary state of a clump can also be represented by the most evolved core within it. We find that nearly all the clumps (such as sources 25 and 63 in Fig. 2) with their most evolved cores in hot molecular core phase or even earlier phases show very good HF morphology. Some clumps (such as sources 44 and 71 in Fig. 2) harbouring UC H II regions also show robust HF morphology, indicating that these UC H II regions are still confined by the dense gas in hub regions. As shown in Fig. 3, expanding H II regions excited by formed proto-clusters will disperse the gas in the hub regions and destroy the HFSs eventually. However, we also notice that those clumps associated with expanding UC H II regions or even more evolved H II regions can still sustain very good filamentary morphology, as shown in Fig. 3.

To conclude, stellar feedback from H II regions gradually destroys the HFSs as proto-clusters evolve.

3.3 Velocity gradients along the longest filaments

Fig. 6 shows the intensity-weighted velocity (moment 1) and integrated intensity (moment 0) of $H^{13}CO^+$ J = 1-0 line emission along the longest filaments in four exemplar sources. Velocity and
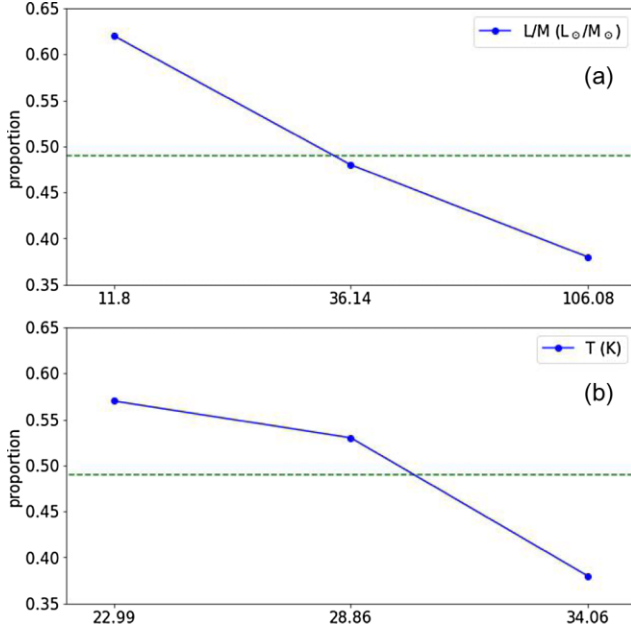
Figure 5. Proportion of ATOM sources with HF morphology in three groups divided by *L/M* and temperature *T*. (a) The bottom *x*-axis represents the average value of *L/M* for all of sources in each group; (b) the bottom *x*-axis is the average value of *T*. Dashed lines mark the proportion of HFSs with good morphology for all of ATOMS sources.

density fluctuations along these filaments are seen, which are likely caused by dense structures embedded in these filaments. The density and velocity fluctuations along filaments may indicate oscillatory gas flows coupled to regularly spaced density enhancements that probably form via gravitational instabilities (Henshaw et al. 2020). We will do a more detailed analysis of this phenomenon in a forthcoming paper.

On the other hand, one can see clear velocity gradients along the longest filaments. We firstly estimate two velocity gradients between velocity peaks and valleys at the two sides of the strongest intensity peaks of $H^{13}CO^+$ emission (i.e. the centre of the gravity potential well), as marked by the vertical dashed lines in Fig. 6, and ignored local velocity fluctuation. We also derive additional velocity gradients over a smaller distances around the strongest intensity peaks of $H^{13}CO^+$ emission for some very long filaments (such as source 25 in the lower panels of Fig. 6). We note that the strongest intensity peaks of $H^{13}CO^+$ emission coincide with the brightest 3-mm cores or hub regions in those HFSs.

In this work, we mainly focus on the longest filaments, which are the skeletons of the clumps. We did not study the other shorter filaments because not all shorter filaments are connected to the hubs. The shorter filaments will be investigated in future works. However, since we have a large sample, the total number of filaments in our analysis is still considerable from a statistical point of view. Fig. 7a shows the distribution of velocity gradients for all sources. The mean value and median value of velocity gradients are 8.71 and 5.54 km s^{-1} pc^{-1}, respectively. Statistically we can see
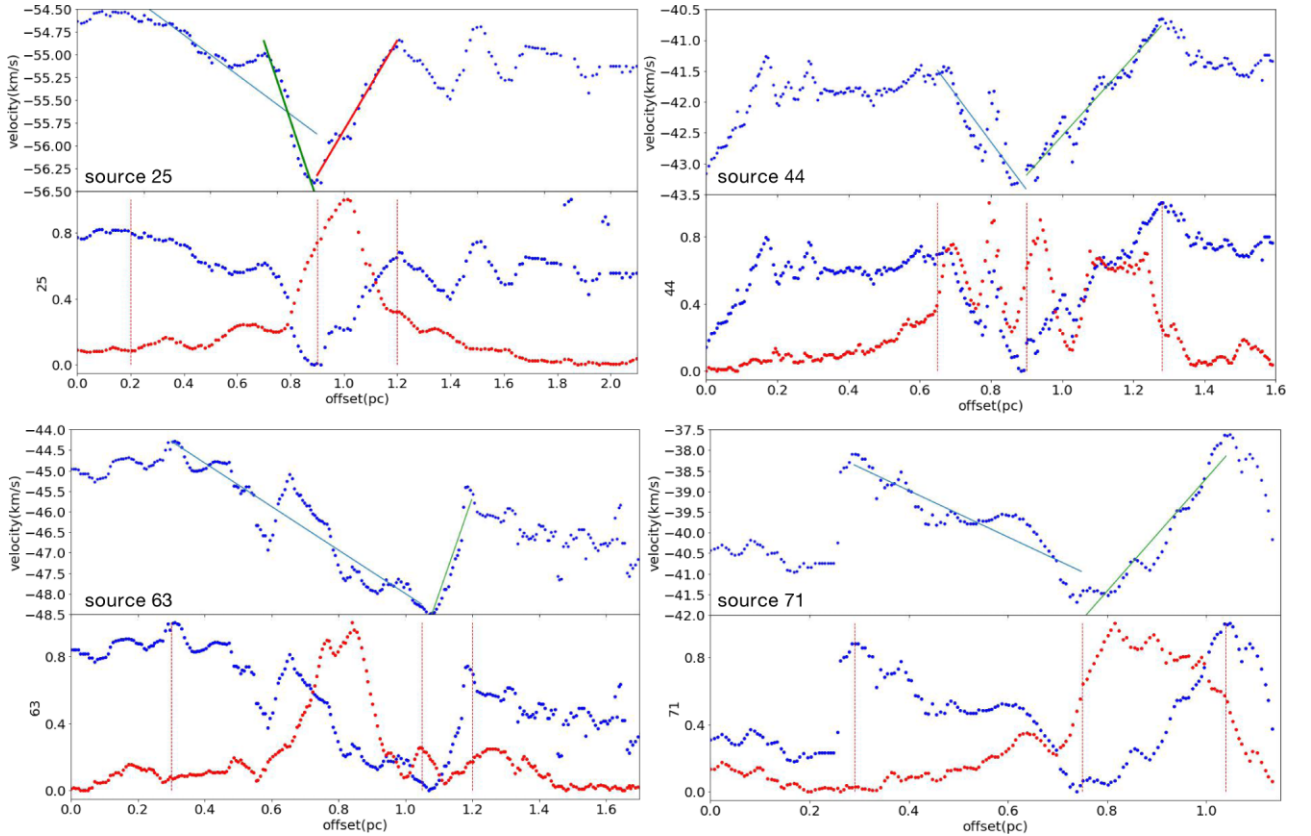
Figure 6. The distributions of velocity and intensity along the longest filament in four exemplar sources. Upper panel for each source: Velocity gradients are fitted in the ranges defined by the red vertical dashed lines, and straight lines show the linear fitting results. Lower panel for each source: Blue and red dotted lines show the normalized velocity and intensity, respectively. The plots for all ATOMS sources are shown in the supplementary material.
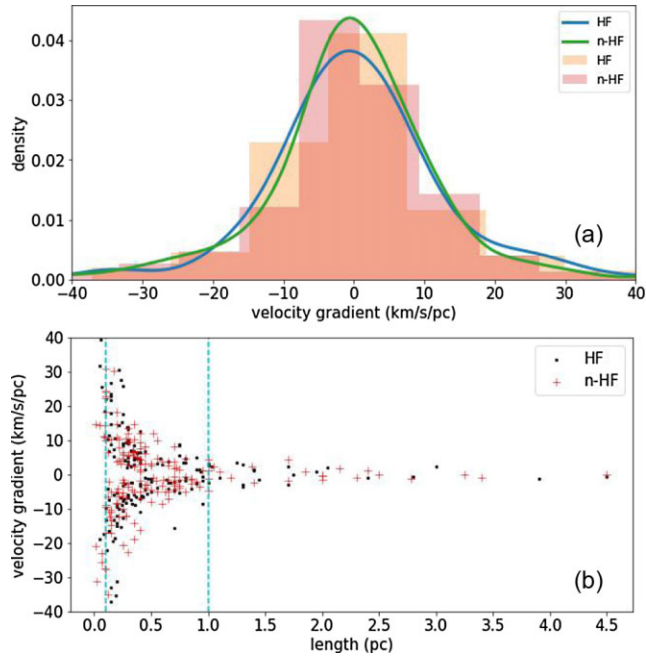
Figure 7. (a) The distribution of velocity gradients along the longest filaments for all of ATOMS sources. (b) Velocity gradient versus the length over which the gradient has been estimated. Black dots and red plus signs represent the velocity gradients of HF sources and non-HF (n-HF) sources. Two cyan dashed lines mark the positions of 0.1 and 1 pc.

approximately symmetric positive and negative velocity gradients in the distribution.

Figs 7b and 8 show velocity gradients as a function of the filament lengths over which the gradients have been estimated. There is no significant difference in velocity gradients among filaments with or without hubs. This may indicate that the physical drivers that generate the kinematics, such as filamentary accretion at different scales, are the same for filaments in various systems. We find that velocity gradients are very small at scales larger than 1 pc relative to small scales (<1 pc), probably hinting for the existence of inertial inflow at large scales driven by turbulence (Padoan et al. 2020), or by large-scale gravitational collapse (Gómez & Vázquez-Semadeni 2014; Vázquez-Semadeni et al. 2019), which compresses and pressurizes the filament, analogously to the compression of the innermost parts of a core by the infall of the envelope (Gómez, Vázquez-Semadeni & Palau 2021). In the case of the filament, this pressure, together with the gravitational pull from the hub, may trigger the longitudinal flow. However, this can also originate from the natural attenuation of the gravitational pull from the hub at large distances from it along the filament, or by the combined gravity of the hub and the interior parts of the filament (cf. Section 4.1). This is evidenced by Fig. 8b, which shows that the variation of velocity gradients on large scales more or less follow the trend at small scales.

Below ~1 pc, velocity gradients dramatically increase as filament lengths decrease, indicating that gravity dominates gas inflow at such small scales where gas is being accumulated in dense cores or hub regions. The large velocity gradients, however, could be overestimated due to the complicated line emission profiles in hub regions. Although the $H^{13}CO^{+}$ J = 1-0 spectral lines over the mapping areas of the majority (75 per cent) of sources in the sample are singly peaked, we noticed asymmetric profiles or even double-peak profiles in lines towards the densest regions of some sources. These complicated line profiles may lead to high velocity gradients
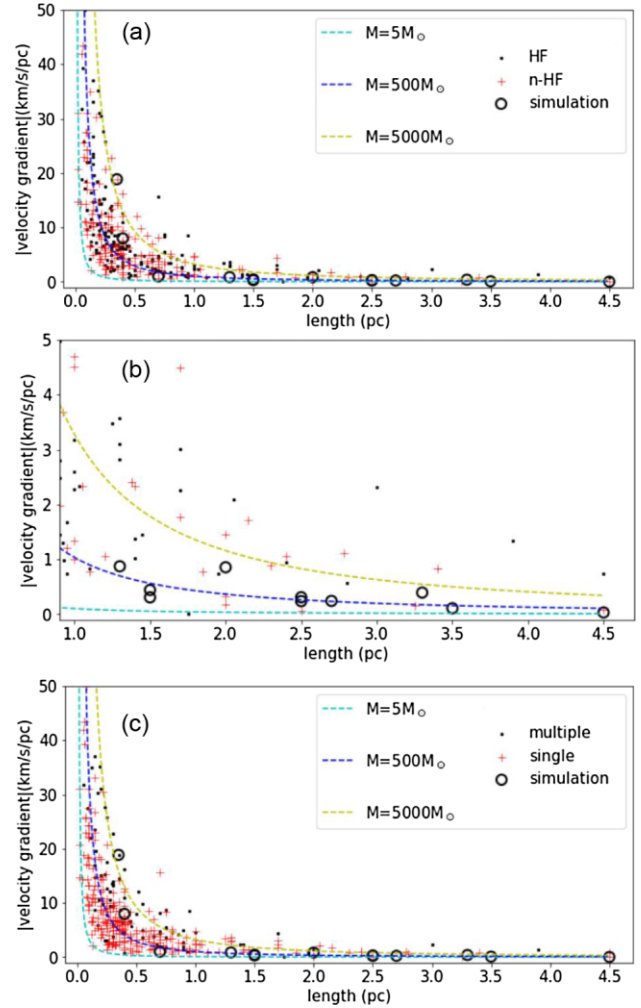

Figure 8. (a) Velocity gradient versus the length over which the gradient has been estimated for all sources. The colour lines show free-fall velocity gradients for comparison. For the free-fall model, cyan, blue, and yellow lines denote masses of 5, 500, and 5000 $M_{\odot}$, respectively. Black circles represent the velocity gradients fitted by simulation data, as shown in Fig. 10. (b) A blow-up of the region with lengths >1 pc in panel a. (c) Same as in panel a, but sources showing singly peaked profiles (red crosses) and multiple-peaked profiles (black dots) in $H^{13}CO^{+}$ line emission in hub regions are plotted separately.

estimated from moment 1 maps near hub regions. Therefore, one should be very cautious about these exceptionally high velocity gradients (in several tens of km s^{-1}). We note that this issue cannot be dealt with by simply fitting the spectra with multiple velocity components because they are more likely caused by the complicated gas motions in the hub regions rather than clearly separated velocity-coherent substructures. In Fig. 8c, we separate the sources that show multiple peaks in $H^{13}CO^{+}$ emission lines from those sources showing singly peaked line profiles. From this plot, we found that the effect caused by the complicated line profiles in hub regions is not a severe problem in statistics, and the trend in the relation between velocity gradients and filament lengths is not changed.

In a recent review work by Hacar et al. (2022), they also found similar trend of the variation of velocity gradients as a function of filament lengths as we witnessed here (Fig. 8). However, they did not include such massive HFSs from high-resolution interferometric observations in their study.

4 DISCUSSION

4.1 From gas inflow to infall along filaments

In observations, velocity gradients along filaments are often interpreted as evidence for gas inflow along filaments (Kirk et al. 2013; Liu et al. 2016a; Williams et al. 2018; Yuan et al. 2018; Chen et al. 2019, 2020b; Pillai et al. 2020).

As mentioned above, the longitudinal flow along the filaments may be due to either a pressure-driven flow or to self-gravity, or a combination thereof. However, each of these possibilities in turn splits in two possible subcases. In the case of the inertial flow, it can be driven by the large-scale turbulent ram pressure, as suggested by Padoan et al. (2020), or to compression by a cloud-scale gravitational contraction, as suggested in the GHC model of Vázquez-Semadeni et al. (2019). On the other hand, if due to self-gravity, it can be dominated by the hub, or by the filament, or both. We consider these possibilities in the Appendix B, and find that longitudinal velocity profile can be naturally explained by the filament's self-gravity.

4.1.1 Longitudinal flow along filaments in simulations

This idea of longitudinal flows along filaments can also be tested in simulations.

Gómez & Vázquez-Semadeni (2014) performed SPH simulations of the formation of a molecular cloud from a convergent flow of diffuse gas. Long filaments with lengths up to 15 pc are formed in the cloud as a consequence of anisotropic, gravitationally driven contraction flow. Fig. 9 presents the density and density-weighted velocity maps of one cloud in their simulation, viewed from three different angles. The cloud exhibits clear filamentary morphology as viewed along *z*-axis or *x*-axis. However, the filament morphology is not obviously seen in the *x*–*z* plane. This indicates that projection effect in observations cannot be ignored in interpreting filament properties. Since the longest filaments in our observations have large aspect ratios, these filaments in our studies do not seem to have extreme inclination angles.

Gómez & Vázquez-Semadeni (2014) witnessed clear longitudinal inflow along filaments in their simulations. Fig. 10 presents the distributions of density and density-weighted velocity along the skeletons of filaments in their simulation. Density and velocity fluctuations are also seen in these simulated filaments. In addition, clear velocity gradients at both large scale (>1 pc) and small scale (<1 pc) are also seen around density peaks. These patterns are remarkably similar to our observational results as seen in Fig. 6. We also derived the overall velocity gradients and local velocity gradients for this simulated filament. In general, the local velocity gradients around density peaks are much larger than the overall velocity gradients at large scales no matter how the filament orients with different inclination angles. The velocity gradients in simulated data are more or less consistent with those in our observations as seen in Fig. 8. This consistency strongly suggests that the velocity gradients along the longest filaments in ATOMS sources are likely caused by longitudinal inflow.

In addition, large-scale velocity gradients perpendicular to the main filament exist across the whole cloud in simulations as seen in the velocity maps of Fig. 9. This indicates that the filament itself is formed due to a convergent flow of diffuse gas in its environment. Velocity gradients perpendicular to filaments are also seen in ATOMS sources as shown in the moment 1 maps of Fig. 2. In a thorough case study of an ATOMS source, G286.21 + 0.17, Zhou et al. (2021) revealed prominent velocity gradients perpendicular to the major

axes of its main filaments, and argued that the filaments are formed due to large-scale compression flows, possibly driven by nearby H II regions and/or cloud-scale gravitational contraction.

4.1.2 Gas infall near hub regions or dense cores

Considering projection effects, the filament lengths would approximate the distances to the centres of mass concentrations (hubs or cores). Therefore, the velocity gradient measured along a filament can be treated as velocity gradient at a contain distance from the centre of gravity potential well. As shown in Figs 7b and 8, velocity gradients dramatically increase as filament lengths decrease at scales smaller than 1 pc. This indicates that the hub's or core's gravity dominates gas flow at such small scales. The observed velocity gradients can be compared with that of free-fall. The free-fall velocity gradient is

$$\nabla V_{\rm free} = -\frac{\rm d}{{\rm d}R}\sqrt{\frac{2GM}{R}} = \sqrt{\frac{GM}{2R^3}}, \tag{1}$$

where M is the mass of the gas concentrations (hubs or cores) and R is the distance to their gravity potential centres. Since the sizes of hubs or cores are far smaller than the filament lengths, here we treat the hubs or cores as point objects. As seen from Fig. 8, the observed velocity gradients roughly follow the free-fall models at small scales, indicating the existence of gas infall governed by the gravity of the hub, or of dense cores located along filaments, in their immediate surroundings. We note that free-fall model may not be realistic, and we also did not consider the masses of filaments themselves. However, this simple comparison indicates that gravity could dominate gas infall at small scales.

4.1.3 The time-scale of filamentary accretion

Below we estimate the gas accretion time-scale of the longest filaments in the ATOMS proto-clusters. Assuming that the velocity gradient along filament is caused by gas inflow, the mass inflow rate ($\dot{M}_\parallel$) along the filament can be estimated by

$$\dot{M}_\parallel = \frac{\nabla V_{\parallel,{\rm obs}}M}{\tan(\alpha)}, \tag{2}$$

where $\nabla V_{\parallel,\,{\rm obs}}$ is the velocity gradient along the filament, M is the filament mass, and α is the inclination angle of the filament relative to the plane of the sky (Kirk et al. 2013). The gas accretion time $t_{\rm inflow}$ scale is then given by

$$t_{\rm inflow} = \frac{M}{\dot{M}_\parallel} = \frac{\tan(\alpha)}{\nabla V_{\parallel,{\rm obs}}}. \tag{3}$$

In calculating $t_{\rm inflow}$, we simply take α equalling to 45° because the longest filaments do not seem to have extreme inclination angles. Therefore, the correction factor for $t_{\rm inflow}$ considering projection effect should be only a factor of a few. The mean value and median value for the gas accretion time are 0.25 and 0.16 Myr, respectively.

We plot $t_{\rm inflow}$ as a function of filament length $d_{\rm fila}$ (over which the velocity gradient is estimated) in Fig. 11. From this figure, we find that $t_{\rm inflow}$ is tightly correlated with $d_{\rm fila}$ in spite of the large data scatter. The correlation can be well fitted by a nearly linear relation:

$$t_{\rm inflow} = 0.49(d_{\rm fila}/{\rm pc})^{0.97}{\rm Myr}. \tag{4}$$

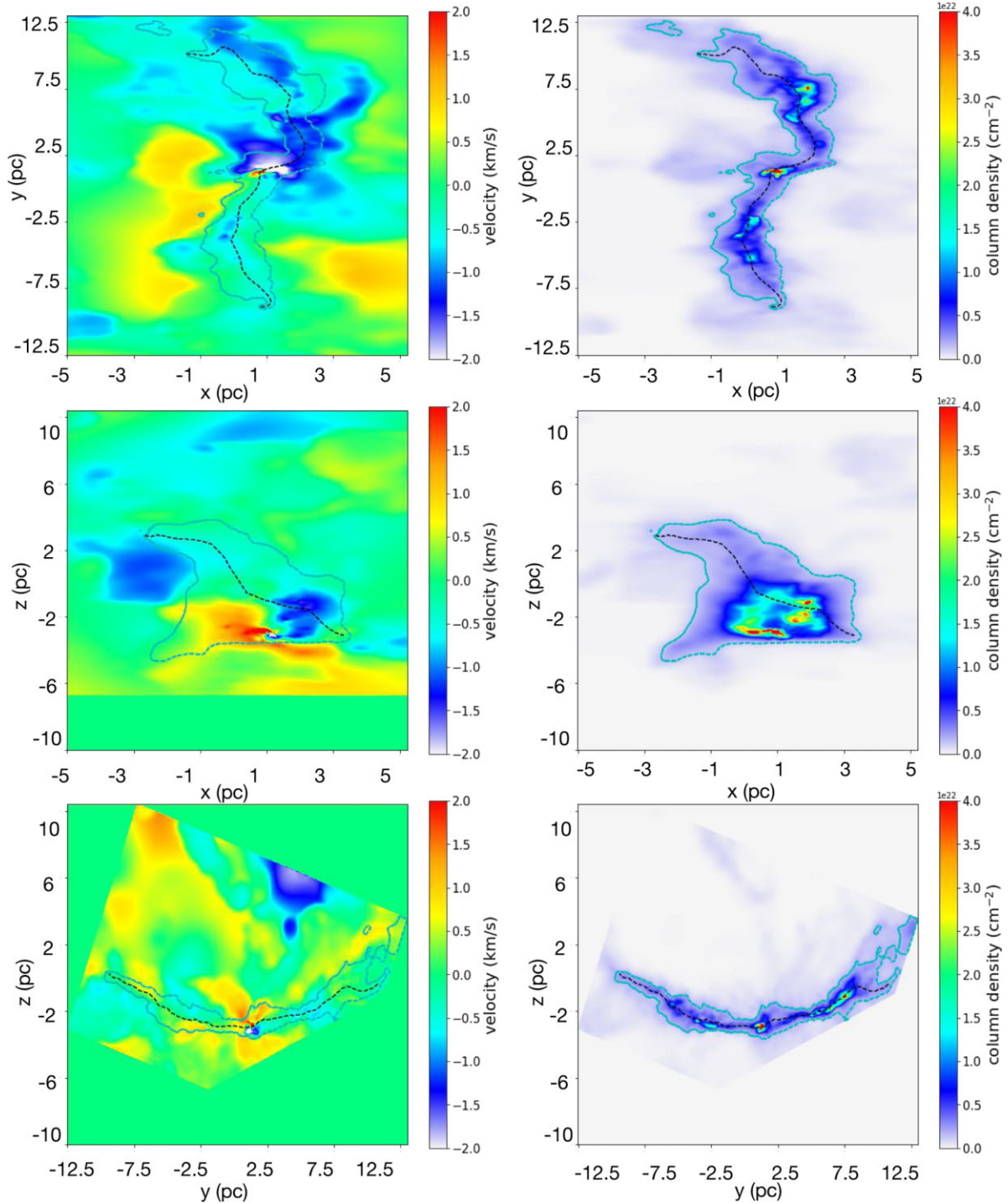The slope 0.97 is very close to 1 with a correlation coefficient r = 0.75.

Figure 9. The distributions of velocity and intensity in three projection planes of 3D SPH simulation in Gómez & Vázquez-Semadeni (2014). Blue dashed lines show ~4σ column density contours, black dashed line represent the longest filament identified by FILFINDER according to the column density map.

4.2 Comparison with theoretical models

There are several popular models for explaining high-mass formation. However, none of them has been fully proven.

The turbulent-core model (McKee & Tan 2003; Krumholz, Klein & McKee 2007) assumes that the formation of a massive star starts from the collapse of a massive prestellar core, which is the gas reservoir for the final stellar mass. However, the prevalent feature of HFSs and potential large-scale converging gas inflows along filaments at scales from ~0.1 to several pc discovered in this work support the idea that the gas reservoirs for high-mass star formation may not be pre-existing massive turbulent cores. Rather, the hubs and dense cores themselves may accumulate most of their masses through large-scale filamentary accretion.

The 'clump-fed' models, such as competitive-accretion model (Bonnell et al. 1997, 2001), inertial-inflow model (Padoan et al. 2020), and GHC model (Vázquez-Semadeni et al. 2009, 2019;
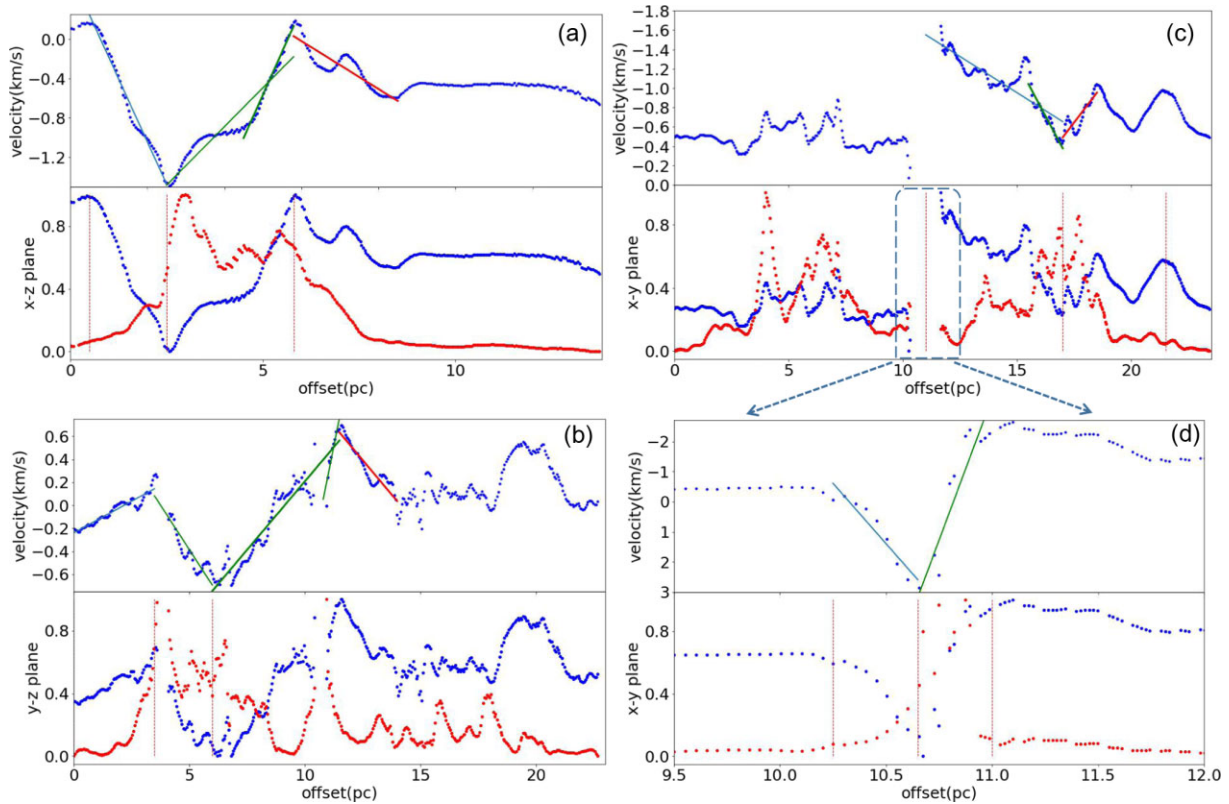
Figure 10. The distributions of velocity and intensity along the longest filament marked by black dashed lines in Fig. 9. Their features are the same with Fig. 6. The d panel shows the velocity shear region marked in c panel by blue dashed box.
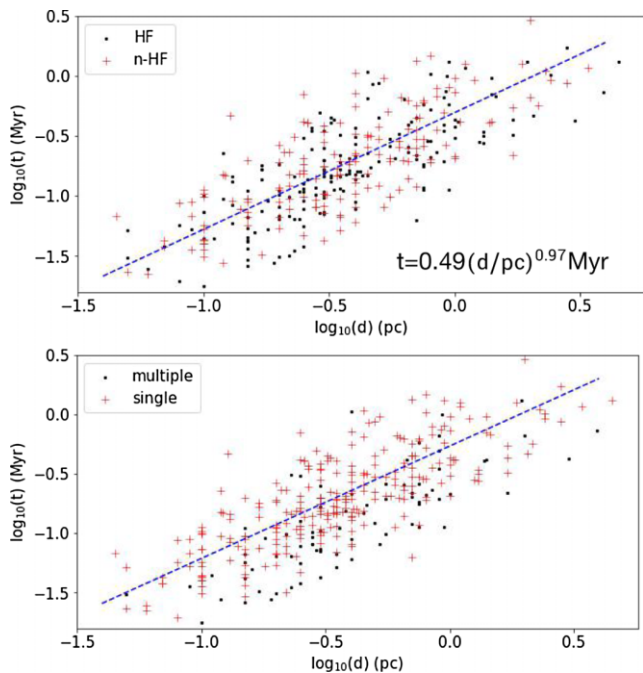

Figure 11. Gas accretion time-scale t_{inflow} versus filament length d_{fila} over which the velocity gradient is estimated. (a) HFS (black dots) and non-HFSs (red crosses); (b) sources (red crosses) showing singly peaked profiles of H^{13}CO$^+$ line emission in hub regions and sources (black dots) showing multiple-peaked profiles.

Ballesteros-Paredes et al. 2011; Hartmann, Ballesteros-Paredes & Heitsch 2012; Vázquez-Semadeni, González-Samaniego & Colín 2017), assume that high-mass stars are born with low stellar masses but grow to much larger final stellar masses by accumulating mass from large-scale gas reservoirs beyond their natal dense cores. In these models, large-scale converging flows or global collapse of clumps are required to continuously feed mass into the dense cores. However, the method of accretion or accumulating material in these models is different.

The competitive-accretion model only accounts for mass accretion due to the gravity of the growing proto-stars (Bondi–Hoyle accretion), neglecting the pre-existing inflow at the larger scales as we observed here.

In the inertial-inflow model, the prestellar cores that evolve into massive stars have a broad mass distribution but can accrete gas from pc scales through large-scale converging flows (Padoan et al. 2020). This model predicts that the pc-scale region around a prestellar core is turbulent and gravitationally unbound (Padoan et al. 2020). However, in observations, most Galactic pc-scale massive clumps seem to be gravitationally bound no matter how evolved they are (Liu et al. 2016b; Urquhart et al. 2018). The inertial-inflow model also predicts that the net inflow velocity in inflow region is generally much smaller than the turbulent velocity and is not dominated by gravity (Padoan et al. 2020). This is contrary to our results as shown in Fig. 7b, from which one can see that gravity may start to dominate gas infall at scales smaller than ∼1 pc.

The GHC model advocates a picture of molecular clouds in a state of hierarchical and chaotic gravitational collapse (multiscale infall motions), in which local centres of collapse develop throughout the cloud while the cloud itself is also contracting (Vázquez-Semadeni
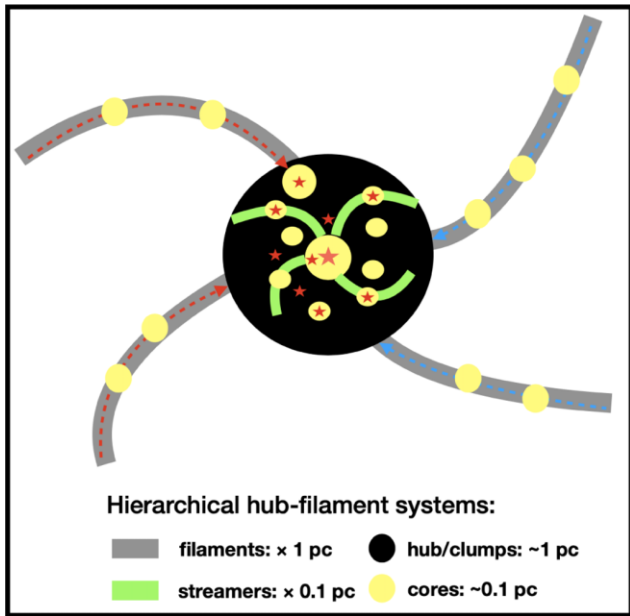
Figure 12. Schematic diagram of self-similar hierarchical HFS at different scales.

et al. 2019). This model predicts anisotropic gravitational contraction with longitudinal flow along filaments at all scales. In our work, we found that velocity gradients along filaments are small at scales larger than ~1 pc, indicating that gravity may not dominate gas flow at such large pc scale. However, both GHC model and inertial-inflow predict small velocity gradients at large scales, and they are not distinguishable in this aspect.

In conclusion, the prevalent HFSs found in proto-clusters favours the pictures advocated by either GHC or inertial-inflow scenarios, which emphasize longitudinal flow along filaments. However, here we argue that gas infall at scales smaller than ~1 pc is likely dominated by the gravity of the hub, while velocity gradients are very small at scales larger than ~1 pc, probably suggesting the dominance of either pressure-driven inflow, which may be driven either by large-scale turbulent motions (inertial inflow) or large-, cloud-scale collapse, or else the self-gravity of the filament. Similar results can also be seen in Liu et al. (2022a, 2022b).

As discussed in Section 3.2.1, we find that HF structures can exist at various scales from 0.1 to several pc in very different Galactic environments as described in Fig. 12. Interestingly, below the 0.1-pc scale, slender structures similar to filaments, such as spiral arms, have also been detected in the surroundings of high-mass protostars (Liu et al. 2015; Maud et al. 2017; Izquierdo et al. 2018; Chen et al. 2020a; Sanhueza et al. 2021). Therefore, self-similar HFSs and filamentary accretion seem to exist at all scales (from several thousand au to several pc) in high-mass star-forming regions. This paradigm of hierarchical HF like systems should be considered in any promising model for high-mass star formation.

4.3 Caveats in this work

In this work, we identified filaments using $H^{13}CO^+$ J = 1-0 data with the FILFINDER algorithm. However, the way that individual filaments have been defined is completely dependent on the algorithm that has been used. In FILFINDER algorithm, there are two key parameters, skel-thresh and branch-thresh, which affect the number

of identified skeletons and branches very much. Although we carefully adjusted these parameters for individual sources, we cannot guarantee that the filament networks identified in our study ideally unveil the underlying hierarchical structures of the clumps. However, the identification of the longest filament skeletons is not greatly affected by choosing different parameters. Therefore, we mainly investigate the gas kinematics of the longest filaments in this work.

In addition, although $H^{13}CO^+$ J = 1-0 is a good tracer of dense gas, it may not be able to trace the highest density gas due to its relatively low critical density ($\sim 2 \times 10^4$ cm^{-3}). Future studies with various gas tracers that have different excitation conditions could be helpful to fully reveal the gas distribution within these massive clumps.

The other caveat in this work is about the classification of HFSs. The exact number of HFSs in the sample is very dependent on the definition. The classification of HFSs by eye is also not completely reliable. However, from a statistical view with such a large sample, our analysis should not be greatly affected by these issues.

In this work, we interpret velocity gradients along filaments as evidences for gas inflow or gas infall. Basically, this may be true because most clumps in the sample are gravitationally bound with small virial parameters (Liu et al. 2016b, 2020b). However, we have ignored the effects of stellar feedback such as outflows, radiation and/or stellar winds in H II regions, which may cause outward motions along or across filaments. The complex interplay between gas inflow and stellar feedback will be investigated thoroughly in future works.

5 SUMMARY

We have studied the physical properties and evolution of HFSs in a large sample of proto-clusters that were observed in the ATOMS survey. The main results of this work are as follows:

(1) We use the moment 0 maps (integrated intensity maps) of the $H^{13}CO^+$ J = 1-0 emission and the FILFINDER algorithm to identify filaments in ATOMS sources. We find that filaments are nearly ubiquitous in proto-clusters. With our strict definition, 49 per cent of sources are classified as HFSs.

(2) We find that HF structures can exist not only in small-scale (~0.1 pc) dense cores but also in large-scale clumps/clouds (~1–10 pc), suggesting that self-similar HFSs at various scales are crucial for star and stellar cluster formation in various Galactic environments.

(3) We find that the proportion of HFSs decreases as T_d and L/M increase, indicating that stellar feedback from H II regions gradually destroys the HFSs as proto-clusters evolve. HFSs in clumps containing H II regions may have been destroyed by stellar feedback as H II regions expand. Therefore, we argue HFSs are crucially important in the formation and evolution of massive proto-clusters.

(4) The longest filaments in ATOMS sources show clear velocity gradients. The approximately symmetric distribution of positive and negative velocity gradients strongly indicates the existence of converging gas inflows along filaments. We also find that velocity gradients are very small at scales larger than ~1 pc, probably suggesting the dominance of pressure-driven inertial inflow, which can originate either from large-scale turbulence or from cloud-scale gravitational contraction. Below ~1 pc, velocity gradients dramatically increase as filament lengths decrease, indicating that the hub's or core's gravity dominates gas infall at such small scales. Assuming that the velocity gradients along filaments are caused by gas inflow, we find that gas inflow time-scale t_{inflow} is linearly

correlated with filament length d_{fila}. Our observations indicate that high-mass stars in proto-clusters may accumulate most of their mass through longitudinal inflow along filaments.

(5) We argue that any promising models for high-mass star formation should include self-similar HFSs and filamentary accretion at all scales (from several thousand au to several pc).

DATA AVAILABILITY

The data underlying this article are available in the article and in ALMA archive.

REFERENCES

André P., Di Francesco J., Ward-Thompson D., Inutsuka S. I., Pudritz R. E., Pineda J. E., 2014, in Beuther H., Klessen R. S., Dullemond C. P., Henning T., eds, Protostars and Planets VI. Univ. Arizona Press, Tucson, p. 27

André P. et al., 2016, A&A, 592, A54

Ballesteros-Paredes J., Hartmann L. W., Vázquez-Semadeni E., Heitsch F., Zamora-Avilés M. A., 2011, MNRAS, 411, 65

Benjamin R. A. et al., 2003, PASP, 115, 953

Bergin E. A., Tafalla M., 2007, ARA&A, 45, 339

Beuther H., Ragan S. E., Johnston K., Henning T., Hacar A., Kainulainen J. T., 2015, A&A, 584, A67

Bonnell I. A., Bate M. R., Clarke C. J., Pringle J. E., 1997, MNRAS, 285, 201

Bonnell I. A., Bate M. R., Clarke C. J., Pringle J. E., 2001, MNRAS, 323, 785

Bronfman L., Nyman L. A., May J., 1996, A&AS, 115, 81

Burkert A., Hartmann L., 2004, ApJ, 616, 288

Busquet G. et al., 2016, ApJ, 819, 139

Chen H.-R. V. et al., 2019, ApJ, 875, 24

Chen X. et al., 2020a, Nature Astron., 4, 1170

Chen M. C.-Y. et al., 2020b, ApJ, 891, 84

Chung E. J. et al., 2019, ApJ, 877, 114

Chung E. J. et al., 2021, ApJ, 919, 3

Dewangan L. K., Ojha D. K., Sharma S., Palacio S. d., Bhadari N. K., Das A., 2020, ApJ, 903, 13

Faúndez S., Bronfman L., Garay G., Chini R., Nyman L. Å., May J., 2004, A&A, 426, 97

Gómez G. C., Vázquez-Semadeni E., 2014, ApJ, 791, 124

Gómez G. C., Vázquez-Semadeni E., Palau A., 2021, MNRAS, 502, 4963

Hacar A., Clark S., Heitsch F., Kainulainen J., Panopoulou G., Seifried D., Smith R., 2022, preprint (arXiv:2203.09562)

Hartmann L., Ballesteros-Paredes J., Heitsch F., 2012, MNRAS, 420, 1457

Heitsch F., Burkert A., Hartmann L. W., Slyz A. D., Devriendt J. E. G., 2005, ApJ, 633, L113

Heitsch F., Slyz A. D., Devriendt J. E. G., Hartmann L. W., Burkert A., 2006, ApJ, 648, 1052

Henshaw J. D., Caselli P., Fontani F., Jiménez-Serra I., Tan J. C., 2014, MNRAS, 440, 2860

Henshaw J. D. et al., 2020, Nature Astron., 4, 1064

Issac N., Tej A., Liu T., Varricatt W., Vig S., Ishwara Chandra C. H., Schultheis M., 2019, MNRAS, 485, 1775

Izquierdo A. F., Galván-Madrid R., Maud L. T., Hoare M. G., Johnston K. G., Keto E. R., Zhang Q., de Wit W.-J., 2018, MNRAS, 478, 2505

Kirk H., Myers P. C., Bourke T. L., Gutermuth R. A., Hedden A., Wilson G. W., 2013, ApJ, 766, 115

Koch E. W., Rosolowsky E. W., 2015, MNRAS, 452, 3435

Koyama H., Inutsuka S.-i., 2002, ApJ, 564, L97

Krumholz M. R., Klein R. I., McKee C. F., 2007, ApJ, 656, 959

Li S. et al., 2022, ApJ, 926, 165

Lin C. C., Mestel L., Shu F. H., 1965, ApJ, 142, 1431

Liu H. B., Quintana-Lacaci G., Wang K., Ho P. T. P., Li Z.-Y., Zhang Q., Zhang Z.-Y., 2012, ApJ, 745, 61

Liu H. B., Galván-Madrid R., Jiménez-Serra I., Román-Zúñiga C., Zhang Q., Li Z., Chen H.-R., 2015, ApJ, 804, 37
Liu T. et al., 2016a, ApJ, 824, 31
Liu T. et al., 2016b, ApJ, 829, 59
Liu H.-L. et al., 2017, A&A, 602, A95
Liu H.-L., Stutz A., Yuan J.-H., 2019, MNRAS, 487, 1259
Liu T. et al., 2020a, MNRAS, 496, 2790
Liu T. et al., 2020b, MNRAS, 496, 2821
Liu H.-L. et al., 2021, MNRAS, 505, 2801
Liu H.-L. et al., 2022a, MNRAS, 510, 5009
Liu H.-L. et al., 2022b, MNRAS, 511, 4480
Lu X. et al., 2018, ApJ, 855, 9
McKee C. F., Tan J. C., 2003, ApJ, 585, 850
McMullin J. P., Waters B., Schiebel D., Young W., Golap K., 2007, in Shaw R. A., Hill F., Bell D. J., eds, ASP Conf. Ser. Vol. 376, Astronomical Data Analysis Software and Systems XVI. Astron. Soc. Pac., p. 127
Maud L. T., Hoare M. G., Galván-Madrid R., Zhang Q., de Wit W. J., Keto E., Johnston K. G., Pineda J. E., 2017, MNRAS, 467, L120
Molinari S., Pezzuto S., Cesaroni R., Brand J., Faustini F., Testi L., 2008, A&A, 481, 345
Molinari S. et al., 2019, MNRAS, 486, 4508
Myers P. C., 2009, ApJ, 700, 1609
Ohashi S., Sanhueza P., Chen H.-R. V., Zhang Q., Busquet G., Nakamura F., Palau A., Tatematsu K., 2016, ApJ, 833, 209
Padoan P., Pan L., Juvela M., Haugbølle T., Nordlund Å., 2020, ApJ, 900, 82
Peretto N. et al., 2013, A&A, 555, A112
Pillai T. G. S. et al., 2020, Nature Astron., 4, 1195
Sanhueza P. et al., 2021, ApJ, 915, L10
Saraceno P., Andre P., Ceccarelli C., Griffin M., Molinari S., 1996, A&A, 309, 827
Schneider N. et al., 2012, A&A, 540, L11
Shimajiri Y. et al., 2017, A&A, 604, A74
Shirley Y. L., 2015, PASP, 127, 299
Smith R. J., Glover S. C. O., Klessen R. S., Fuller G. A., 2016, MNRAS, 455, 3640
Stephens I. W., Jackson J. M., Whitaker J. S., Contreras Y., Guzmán A. E., Sanhueza P., Foster J. B., Rathborne J. M., 2016, ApJ, 824, 29
Urquhart J. S. et al., 2018, MNRAS, 473, 1059
Vázquez-Semadeni E., Ryu D., Passot T., González R. F., Gazol A., 2006, ApJ, 643, 245
Vázquez-Semadeni E., Gómez G. C., Jappsen A. K., Ballesteros-Paredes J., González R. F., Klessen R. S., 2007, ApJ, 657, 870
Vázquez-Semadeni E., Gómez G. C., Jappsen A. K., Ballesteros-Paredes J., Klessen R. S., 2009, ApJ, 707, 1023
Vázquez-Semadeni E., González-Samaniego A., Colín P., 2017, MNRAS, 467, 1313
Vázquez-Semadeni E., Palau A., Ballesteros-Paredes J., Gómez G. C., Zamora-Avilés M., 2019, MNRAS, 490, 3061
Vishniac E. T., 1994, ApJ, 428, 186
Walder R., Folini D., 2000, Ap&SS, 274, 343
Wang P., Li Z.-Y., Abel T., Nakamura F., 2010, ApJ, 709, 27
Wang K., Zhang Q., Wu Y., Zhang H., 2011, ApJ, 735, 64
Williams G. M., Peretto N., Avison A., Duarte-Cabral A., Fuller G. A., 2018, A&A, 613, A11
Yuan J. et al., 2018, ApJ, 852, 12
Zamora-Avilés M., Ballesteros-Paredes J., Hartmann L. W., 2017, MNRAS, 472, 647
Zhang Q., Wang K., Lu X., Jiménez-Serra I., 2015, ApJ, 804, 141
Zhang C. et al., 2022, MNRAS, 510, 4998
Zhou J.-W. et al., 2021, MNRAS, 508, 4639

SUPPORTING INFORMATION

Supplementary data are available at *MNRAS* online.

Figure 1. The $H^{13}CO^+$ spectral grid map for an exemplar source. The background image shows the integrated intensity map.
Figure 2. HFSs in four exemplar sources.

Figure 3. Four ATOMS sources containing expanding H II regions.
Figure 6. The distributions of velocity and intensity along the longest filament in four exemplar sources.

Please note: Oxford University Press is not responsible for the content or functionality of any supporting materials supplied by the authors. Any queries (other than missing material) should be directed to the corresponding author for the article.

APPENDIX A: DISTANCES AND EVOLUTION OF HFSS

Panel a in Fig. A1 shows the distribution of distances for the ATOMS sample. Panel b in Fig. A1 presents dust temperature (T_d) versus distance for all ATOMS sources, and panel c shows the relation between luminosity-to-mass ratios (L/M) and distances. From these two panels, one can see that T_d and L/M do not depend on distances in the ATOMS sample.

In Fig. A2, we divide ATOMS sources into ten uniformly spaced bins in T_d and L/M, respectively. As shown this figure, the proportion of HFSs decreases with increasing T_d and L/M in general. We noticed that the sources with smallest L/M have less HFSs, which may indicate that HFSs have not been fully developed in the youngest
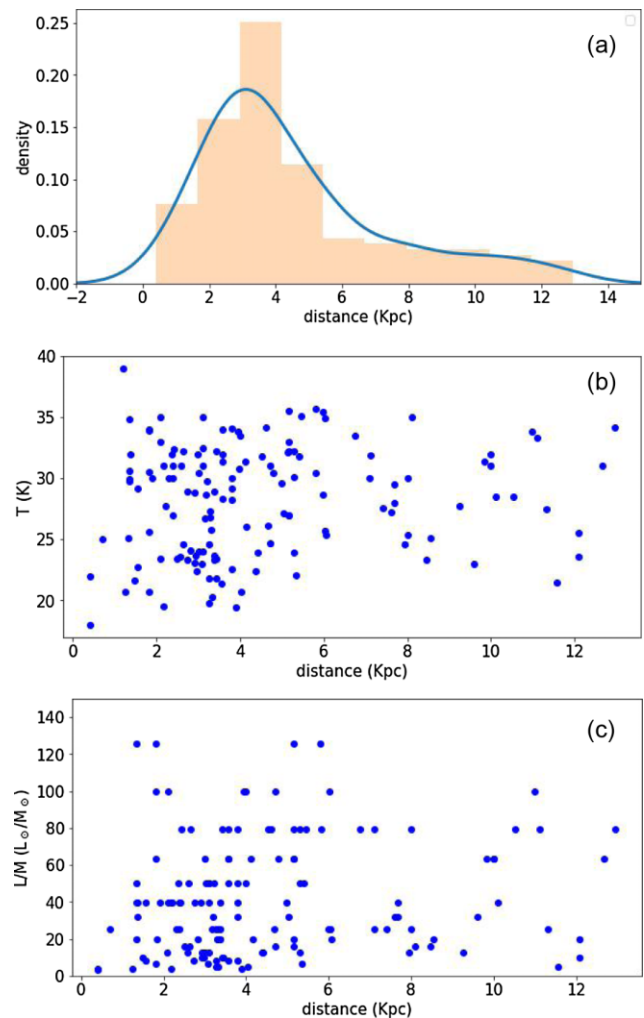

Figure A1. (a) Distance distribution of ATOMS sources. (b) Dust temperature of ATOMS sources versus distance. (c) L/M of ATOMS sources versus distance.
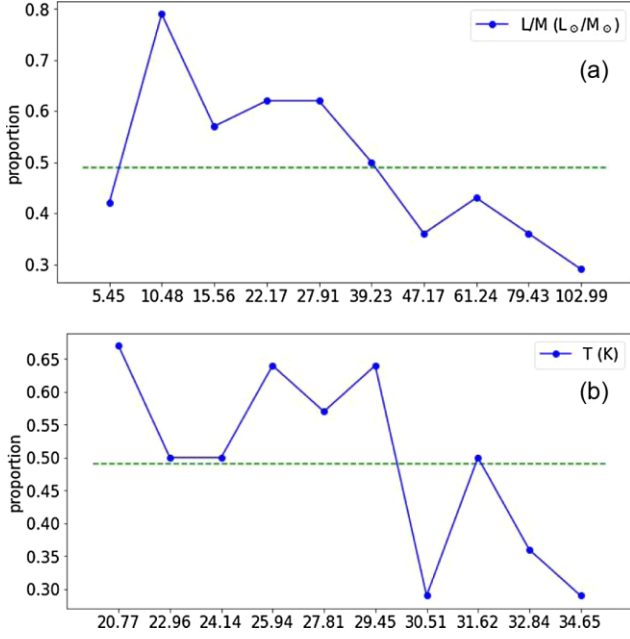
Figure A2. Proportion of ATOM sources with HF morphology divided by *L/M* and temperature *T* in 10 bins. (a) The bottom *x*-axis represents the average value of *L/M* for all of sources in each bin; (b) The bottom *x*-axis is the average value of *T*. Dashed lines mark the proportion of HFSs with good morphology for all of ATOMS sources.

clumps. However, these results should be taken caution because each bin only contains about 14 sources and the statistics with such a small number of sources in each bin may not be significant. Studies with a larger sample of sources with a larger dynamic range in T_d and *L/M* would help further constrain the evolution of HFSs.

APPENDIX B: LONGITUDINAL VELOCITY PROFILE IN THEORY

B1 The longitudinal velocity profile for a constant accretion rate per unit length on to the filament

Let us consider the pressure-driven case first. Without making any assumptions on whether the pressure is due to turbulence or gravitational infall from the cloud scale, let us consider the case of a filament of linear mass density λ, which hosts a longitudinal flow with velocity $v(z)$, where z is the coordinate along the filament. In addition, we assume that the filament is accreting radially from the cloud at a uniform rate per unit length $\dot{\lambda}_0$ throughout its length, so that each cylindrical segment of thickness Δz of the filament accretes mass radially at a rate

$$\dot{M}_{\rm rad} = \dot{\lambda}_0 \, \Delta z. \tag{B1}$$

However, as seen from the intensity (red dotted) lines in Fig. 6, the linear mass density of the filament appears to be roughly constant to zeroth order along the filament. To achieve this constancy, the longitudinal accretion rate λv must increase across Δz by an amount

$$\Delta \dot{M}_{\rm long} = \lambda \Delta v = \dot{M}_{\rm rad} = \dot{\lambda}_0 \, \Delta z. \tag{B2}$$

Since both λ and $\dot{\lambda}_0$ are constants to zeroth order, we the find that, to this order,

$$\Delta v \propto \Delta z, \tag{B3}$$

which is consistent with the linear fits to the velocity seen in Fig. 6.

B2 The longitudinal velocity profile due to the filament's self-gravity

Let us consider an infinitely thin filament of uniform linear mass density λ placed between $-L$ and L, away from the gravitational force of the hub or early in the filament evolution, i.e. before the hub formation. Consider also a gas parcel within the filament at z and, for simplicity, assume that $z > 0$. The gravitational force experienced by the gas parcel is given by,

$$F(z) = \int_{-L}^{2z-L} \frac{G\lambda {\rm d}z'}{(z' - z)^2}$$
$$= \frac{-2G\lambda z}{L^2 - z^2}, \tag{B4}$$

(since the force due to the $[z, L]$ filament segment is balanced by the symmetrical $[2z - L, z]$ one. See Burkert & Hartmann 2004 for a more detailed analysis). The work ΔW exerted by this force on to the parcel will give it a kinetic energy K. Assuming that the gas parcel starts at $z_0 \ll L$ at zero velocity, then $\Delta W = K$ implies

$$v^2(z) = 2G\lambda \left(z_0^2 - z^2 \right), \tag{B5}$$

and the velocity of the gas parcel will be approximately linear with z.

Notice that in this simple model, the velocity vector at either side of the filament centre should point to $z = 0$, so it should be interpreted as modelling the flow associated with individual collapse centres embedded within the filament. In this sense, the velocity profile in eq. (B5) calculated for a finite filament is applicable to segments surrounding individual collapses within the filament as a whole, highlighting the self-similar nature of the process.

[1] *National Astronomical Observatories, Chinese Academy of Sciences, Beijing 100101, People's Republic of China*

[2] *School of Astronomy and Space Science, University of Chinese Academy of Sciences, Beijing 100049, People's Republic of China*

[3] *Shanghai Astronomical Observatory, Chinese Academy of Sciences, 80 Nandan Road, Shanghai 200030, People's Republic of China*

[4] *Department of Astronomy, The University of Texas at Austin, 2515 Speedway, Stop C1400, Austin, TX 78712-1205, USA*

[5] *Departamento de Astronomía, Universidad de Chile, Camino el Observatorio 1515, Las Condes, Santiago, Chile*

[6] *Jet Propulsion Laboratory, California Institute of Technology, 4800 Oak Grove Drive, Pasadena, CA 91109, USA*

[7] *Instituto de Radioastronomía y Astrofísica, Universidad Nacional Autónoma de México, Antigua Carretera a Pátzcuaro # 8701, Ex-Hda. San José de la Huerta, Morelia, Michoacán, C.P. 58089, México*

[8] *Department of Astronomy, Yunnan University, Kunming 650091, People's Republic of China*

[9] *Departamento de Astronomía, Universidad de Concepción, Casilla 160-C, Concepción, Chile*

[10] *Kavli Institute for Astronomy and Astrophysics, Peking University, Haidian District, Beijing 100871, People's Republic of China*

[11] *Department of Physics, University of Helsinki, PO Box 64, FI-00014 Helsinki, Finland*

[12] *Yunnan Observatories, Chinese Academy of Sciences, 396 Yangfangwang, Guandu District, Kunming 650216, People's Republic of China*

[13] *Chinese Academy of Sciences South America Center for Astronomy, National Astronomical Observatories, CAS, Beijing 100101, People's Republic of China*

[14] *Departamento de Astronomía, Universidad de Chile, Casilla 36-D, Santiago, Chile*

[15] *NAOC-UKZN Computational Astrophysics Centre, University of KwaZulu-Natal, Durban 4000, South Africa*

[16] *Department of Astronomy, School of Physics, Peking University, Beijing 100871, People's Republic of China*

[17] *Indian Institute of Space Science and Technology, Thiruvananthapuram, Kerala 695547, India*

[18] *Physical Research Laboratory, Navrangpura, Ahmedabad 380009, India*

[19] *Korea Astronomy and Space Science Institute, 776 Daedeokdae-ro, Yuseong-gu, Daejeon 34055, Republic of Korea*

[20] *Institute of Astronomy and Astrophysics, Anqing Normal University, Anqing 246133, People's Republic of China*

[21] *Nobeyama Radio Observatory, National Astronomical Observatory of Japan, National Institutes of Natural Sciences, Nobeyama, Minamimaki, Minamisaku, Nagano 384-1305, Japan*

[22] *Department of Astronomical Science, The Graduate University for Advanced Studies, SOKENDAI, 2-21-1 Osawa, Mitaka, Tokyo 181-8588, Japan*

[23] *Astronomy Department, University of California, Berkeley, CA 94720, USA*

[24] *University of Science and Technology, Korea (UST), 217 Gajeong-ro, Yuseong-gu, Daejeon 34113, Republic of Korea*

[25] *S. N. Bose National Centre for Basic Sciences, JD Block, Sector-III, Salt Lake City, Kolkata 700106, India*

[26] *College of Science, Yunnan Agricultural University, Kunming 650201, People's Republic of China*

[27] *School of Physics and Astronomy, Sun Yat-sen University, 2 Daxue Road, Tangjia, Zhuhai, Guangdong Province, People's Republic of China*

[28] *CSST Science Center for the Guangdong-Hongkong-Macau Greater Bay Area, Sun Yat-Sen University, Guangdong Province, People's Republic of China*

[29] *Laboratory for Space Research, The University of Hong Kong, Hong Kong 000000, People's Republic of China*

[30] *Indian Institute of Science Education and Research (IISER) Tirupati, Rami Reddy Nagar, Karakambadi Road, Mangalam (P.O.), Tirupati 517507, India*

[31] *Center for Astrophysics, Harvard Smithsonian, 60 Garden Street, Cambridge, MA 02138, USA*

[32] *IRAP, Université de Toulouse, CNRS, UPS, CNES, Toulouse 31400, France*

This paper has been typeset from a TEX/LATEX file prepared by the author.